










Ladder-like energy-relaying exciplex enables 100% internal quantum efficiency of white TADF-based diodes in a single emissive layer

Chunmiao Han ¹, Ruiming Du ¹, Hui Xu ¹✉, Sanyang Han ², Peng Ma¹, Jinkun Bian¹, Chunbo Duan ¹, Ying Wei ¹, Mingzhi Sun ¹, Xiaogang Liu ²✉ & Wei Huang ^{3,4}✉

Development of white organic light-emitting diodes based on purely thermally activated delayed fluorescence with a single-emissive-layer configuration has been a formidable challenge. Here, we report the rational design of a donor-acceptor energy-relaying exciplex and its utility in fabricating single-emissive-layer, thermally activated delayed fluorescence-based white organic light-emitting diodes that exhibit 100% internal quantum efficiency, 108.2 lm W⁻¹ power efficiency, and 32.7% external quantum efficiency. This strategy enables thin-film fabrication of an 8 cm × 8 cm thermally activated delayed fluorescence white organic light-emitting diodes (10 inch²) prototype with 82.7 lm W⁻¹ power efficiency and 25.0% external quantum efficiency. Introduction of a phosphine oxide-based acceptor with a steric group to the exciplex limits donor-acceptor triplet coupling, providing dual levels of high-lying and low-lying triplet energy. Transient spectroscopic characterizations confirm that a ladder-like energy relaying occurs from the high-lying triplet level of the exciplex to a blue emitter, then to the low-lying triplet level of the phosphine oxide acceptor, and ultimately to the yellow emitter. Our results demonstrate the broad applicability of energy relaying in multicomponent systems for exciton harvesting, providing opportunities for the development of third-generation white organic light-emitting diode light sources.

¹Key Laboratory of Functional Inorganic Material Chemistry (Ministry of Education) & School of Chemistry and Material Science, Heilongjiang University, Harbin, PR China. ²Department of Chemistry, National University of Singapore, Singapore, Singapore. ³Key Laboratory of Flexible Electronics & Institute of Advanced Materials, Nanjing Tech University, Nanjing, China. ⁴Frontiers Science Center for Flexible Electronics (FSCFE) & Shaanxi Institute of Flexible Electronics (SIFE), Northwestern Polytechnical University (NPU), Xi'an, China. ✉email: hxu@hlju.edu.cn; chmlx@nus.edu.sg; iamwhuang@nwpu.edu.cn

Considerable effort has recently been devoted to developing high-efficiency, white organic light-emitting diodes (WOLEDs) with compact design and large-area processing capability^{1–3}. Thermally activated delayed fluorescence (TADF), based on purely organic emitters, enables theoretical 100% internal quantum efficiency for both singlet and triplet exciton harvesting^{4–6}. A single-emissive layer (EML) design, comprising blue/yellow emitters or red/green/blue emitters, can simplify WOLED device structure effectively and can meet the demands of large-scale production, quality control, and low cost^{7–9}. However, competition in exciton confinement between various color emitters makes it challenging to control emission color and device efficiency synchronously (Fig. 1)^{10,11}. As an additional constraint, charge-transfer excited states of TADF dyes are highly sensitive to host-dopant interactions^{12–14} and interfacial effects¹⁵. Indeed, there are few reports of high-efficiency, purely TADF-based WOLEDs, among which multiple emissive layers are required to modify exciton allocation by spatially separating two or three host-dopant systems of different emission color^{16–18}.

High-efficiency WOLEDs with single-EML layout requires precise optimization of optical transition and energy transfer (ET) in a multi-emitter-doped host¹⁹. However, the narrow singlet-triplet splitting energy (ΔE_{ST}) of TADF emitters limits energy-level regulation. The singlet-triplet energy gap between the blue and yellow TADF emitters, e.g., bis[4-(9,9-dimethyl-9,10-dihydroacridine)phenyl]sulfone (DMAC-DPS, $S_1/T_1 \approx 2.8$ eV)²⁰ and 2,3,5,6-tetrakis(3,6-di-*t*-butylcarbazol-9-yl)-1,4-dicyanobenzene (4CzTPNBu, $S_1/T_1 \approx 2.2$ eV)⁴, is approximately 0.6 eV, leading to nonradiative deactivation of excitons during energy transfer^{21–23}.

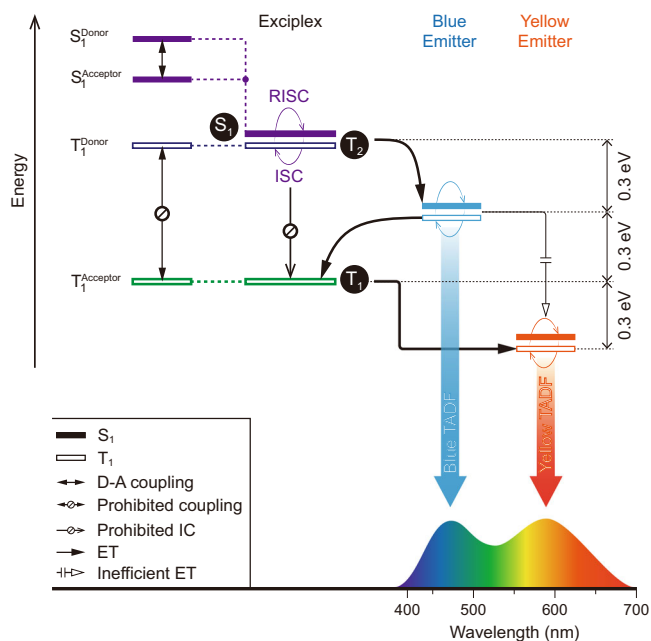


Fig. 1 Proposed energy-relaying mechanism. Exciton allocation in single-emissive-layer, TADF WOLEDs comprising a D–A exciplex host, a blue emitter, and a yellow emitter. Inefficient energy transfer occurs from the exciplex host to the blue emitter and subsequently to the yellow emitter, due to a large energy gap between the blue and yellow emitters (~0.6 eV). The proposed exciplex, based on a high triplet donor and a low triplet acceptor, generates a large triplet gap between a high-lying T_2 and a low-lying T_1 . This design enables efficient ladder-like (~0.3 eV ladder spacing) triplet energy transfer from $T_2 \rightarrow$ blue emitter $\rightarrow T_1 \rightarrow$ yellow emitter. ET, IC, ISC, and RISC refer to energy transfer, internal conversion, intersystem crossing, and reverse ISC, respectively.

Presently, the performance of single-EML, TADF-based WOLEDs is not comparable to that of their phosphorescent counterparts^{24,25}. We reason that a host matrix with dual levels of high-lying and low-lying triplet energy, which match the energy levels of blue and yellow TADF emitters, may improve performance^{23,26}. In contrast, single-molecule-based hosts cannot offer two triplet excited states, due to fast internal conversion to the lowest triplet state (T_1). Therefore, an exciplex host based on a bimolecular donor–acceptor (D–A) system is likely to provide two different triplet states upon appropriate D–A coupling^{27,28}. In principle, a common exciplex comprises a donor and an acceptor with comparable excited energy levels and strong D–A coupling, lowering S_1 and T_1 levels of the exciplex below those of the donor and the acceptor. In contrast, an exciplex design featuring a large triplet energy gap between the donor and the acceptor limits donor–acceptor triplet coupling (Fig. 1)²⁹. This leads to dual triplet levels of the exciplex with an energy difference of 0.6 eV. Therefore, a facile triplet energy transfer process may occur, namely the S_1/T_2 of the exciplex host \rightarrow the S_1/T_1 of blue emitter \rightarrow the T_1 of the exciplex host \rightarrow the T_1 of yellow emitter. As an added benefit, the exciplex host with near-zero ΔE_{ST} can provide additional triplet-singlet conversion and enhance singlet-exciton utilization in the blue-TADF emitter.

As a proof of concept, we designed and synthesized two exciplex hosts, mCP:pDPBITPO and mCP:DpPBITPO, with T_2 and T_1 energy levels of 3.0 and 2.5 eV, based on a high-triplet-energy donor, 1,3-bis(carbazol-9-yl)benzene (mCP, $T_1 = 3.0$ eV) and low-triplet-energy phosphine oxide (PO) acceptors (5-(2-(4-(diphenylphosphoryl)phenyl)-benzimidazol-1-yl)-1,3-phenylene)bis(diphenylphosphine oxide) (pDPBITPO) and (5-(1-(4-(diphenylphosphoryl)phenyl)-benzimidazol-2-yl)-1,3-phenylene)bis(diphenylphosphine oxide) (DpPBITPO) ($T_1 = 2.5$ eV as the average of DMAC-DPS and 4CzTPNBu) (Fig. 2a). Our experimental results show that these two exciplexes promote energy transfer relaying in their DMAC-DPS and 4CzTPNBu-codoped films. A single-EML design based on mCP:pDPBITPO and mCP:DpPBITPO exciplex yielded TADF WOLEDs with a maximum external quantum efficiency (η_{EQE}) of 32.7% and a maximum power efficiency of 108.2 lm W⁻¹, comparable to that of fluorescent lamps.

Results

Exciplex host design. The key molecular design of pDPBITPO and DpPBITPO involves electron-accepting phenylbenzimidazole encapsulated by three diphenylphosphine oxide (DPPO) moieties to provide suitable frontier molecular orbital energy levels and to reduce intermolecular charge-transfer interactions with mCP²⁷ (Fig. 2a). Furthermore, the single-crystal structure of DpPBITPO reveals a twisted configuration of the phenylbenzimidazole group due to steric hindrance of the DPPO moiety (Supplementary Fig. 1). This leads to improved triplet-state structural relaxation, reduced T_1 energy level, and enlarged ΔE_{ST} . Density functional theory (DFT) simulations show locally excited T_1 states of mCP, pDPBITPO and DpPBITPO (Supplementary Fig. 2 and Supplementary Table 1). T_1 energy gaps between the donor and the two acceptors reach ~0.8 eV, which is adequate to restrain D–A triplet exciton interactions. As a result of suppressed triplet D–A electronic coupling, high-lying triplet (T_2) and T_1 states of the exciplexes are localized at mCP and PO acceptors, respectively. Moreover, the energy gaps between the highest occupied (HOMO) and the lowest unoccupied molecular orbital (LUMO) energy levels of mCP and PO acceptors reach ~0.6 eV (Fig. 2b and Supplementary Figs. 3). This suggests strong driving forces of D–A charge transfer upon excitation, giving rise to charge-transfer S_1 states. Effective spin-orbital coupling between the

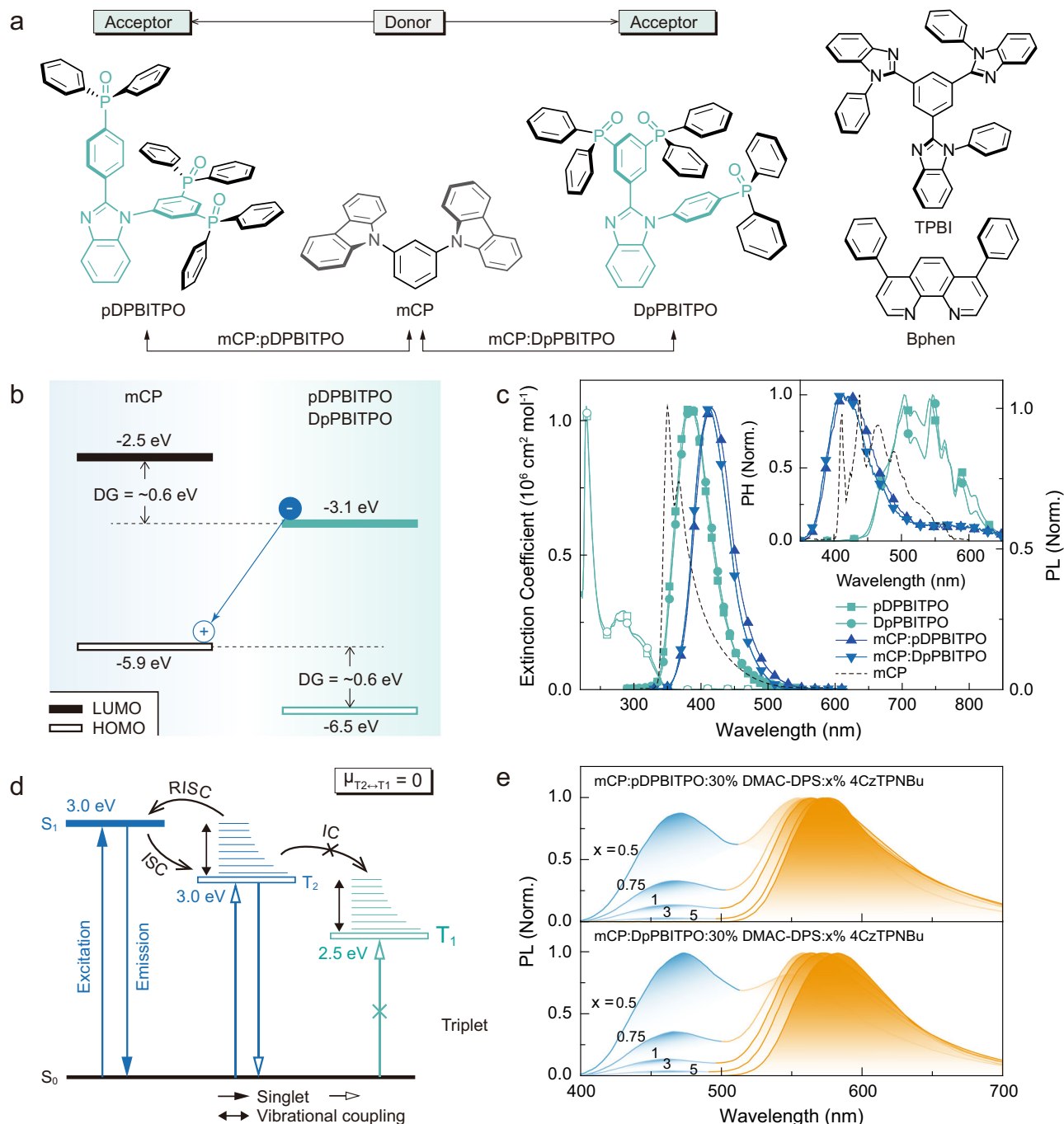


Fig. 2 Structure and energy transition characteristics of the newly developed exciplexes. **a** Molecular structures of one donor and two acceptors used to form exciplexes mCP:pDPBITPO and mCP:DpPBITPO. Two conventional TPBI and BPhen acceptors were used in device fabrication for comparison.

b Frontier molecular orbital (FMO) energy levels of mCP and PO acceptors. Energy gaps of the highest occupied (HOMO) and the lowest unoccupied molecular orbitals (LUMO) between mCP and PO acceptors reach to 0.6 eV, corresponding to the driving force of donor-acceptor electronic coupling (ΔG). **c** Electronic absorption of pDPBITPO and DpPBITPO (hollow dots) and steady-state photoluminescence (PL) and time-resolved phosphorescence (PH) spectra of mCP (dash lines), pDPBITPO, DpPBITPO, mCP:pDPBITPO and mCP:DpPBITPO. Phosphorescence spectra were recorded in the time range of 100–200 μs after excitation. **d** Jablonski energy level diagram of mCP:PO acceptors. The near-zero energy gap between the S₁ and the mCP-induced T₂ of the exciplex facilitates the RISC through electron and vibrational couplings. Separated T₂ and T₁ locations on mCP and PO acceptors restrain the T₂ → T₁ transition through IC. **e** Steady-state PL spectra of mCP:pDPBITPO and mCP:DpPBITPO films doped with DMAC-DPS and 4CzTPNBu at different ratios.

locally excited triplet state and the charge-transfer S₁ state substantially facilitates reverse intersystem crossing (RISC), as evident in the cases of mCP:pDPBITPO and mCP:DpPBITPO (ref. 30). Moreover, PO acceptors are superior to conventional low-triplet-energy acceptors with exposed T₁ states, such as TPBI (T₁ = 2.7 eV) and BPhen (T₁ = 2.6 eV), due to prevention of

collision-induced quenching at the T₁ state by peripheral DPPO groups.

Estimated by 0 → 0 transitions in emission spectra, the T₁ energy levels (2.48 eV) of pDPBITPO and DpPBITPO match well with 4CzTPNBu (2.2 eV), while featuring triplet gaps that are 0.54 eV lower than mCP (T₁ = 3.02 eV). Meanwhile, the S₁

energy levels of the PO acceptors are 3.2 eV, similar to mCP ($S_1 = 3.5$ eV). The deep-blue emissions from co-evaporated mCP:PO acceptor films exhibit a bathochromic shift of 30 nm, corresponding to Gibbs free energy for charge separation beyond 0.2 eV, indicating exciplex formation through D–A electronic coupling (Fig. 2c; Supplementary Figs. 4 and 5; Supplementary Table 2) (ref. 29). The D–A vibrational coupling leads to structureless phosphorescence spectra of mCP:pDPBITPO and mCP:DpPBITPO. The main peaks at 415 nm correspond to the $0 \rightarrow 0$ triplet transition of mCP, namely the mCP-centered $T_2 \rightarrow S_0$ transitions. Therefore, the T_2 levels of the exciplexes (~ 3.0 eV) support efficient energy transfer to DMAC-DPS. Furthermore, the tails of the phosphorescence spectra from 500 to 650 nm overlap with those of the PO acceptors, which can be ascribed to either the $T_1 \rightarrow S_0$ transitions of the exciplexes or to triplet leakage to the T_1 state of acceptors²⁹. Compared to T_1 states located at the PO acceptor, mCP-induced T_2 states are closer to S_1 states, supporting RISC transitions. In the case of weak D–A triplet exciton interactions and mCP-centralized HOMOs, these T_2 states dominate the triplet population. Furthermore, D–A vibrational coupling restrains vibrational perturbation of potential energy surfaces and further alleviates internal conversion from the T_2 to T_1 states (Fig. 2d), closely resembling rigid, intramolecular charge-transfer systems³¹. Despite the decreased photoluminescence quantum yields (ϕ_{PL}) of the exciplexes (<15%) (Supplementary Table 2), the PO acceptor-induced T_1 states can serve as intermediate states to promote triplet energy transfer to 4CzTPNBu.

Photophysical investigation on the energy-relaying process.

The DMAC-DPS (30 wt%) and 4CzTPNBu (5 wt%) singly doped sky-blue and yellow exciplex films (100 nm) showed $\sim 30\%$ and $\sim 65\%$ increased ϕ_{PL} , respectively (Fig. 2e; Supplementary Table 2). These values are still far below the intrinsic values of the dopants ($\sim 95\%$), due to either triplet leakage to the T_1 of the PO acceptors (for DMAC-DPS) or the large energy gap-induced inefficient energy transfer (for 4CzTPNBu). For the doubly doped films of mCP:PO acceptor:30% DMAC-DPS:x% 4CzTPNBu ($x = 0.5-5$), they all achieved ϕ_{PL} values above 90%, approximately the sum of the singly doped films.

The weakly populated bands at 500 nm, observed in the time-resolved contours of mCP:PO acceptor exciplexes due to the phosphorescence from the PO acceptors, could be dramatically enhanced upon doping of 30% DMAC-DPS (Fig. 3a). The triplet energy was transferred from DMAC-DPS to PO acceptors at about 70 ns, followed by the appearance of dominant phosphorescence bands at 150 ns. For mCP:PO acceptor:5% 4CzTPNBu, we only observed blue bands from the exciplexes within 50 ns. The absence of phosphorescence bands indicates that PO acceptors do not participate in triplet energy transfer to 4CzTPNBu due to forbidden $T_2 \rightarrow T_1$ transitions of the exciplexes. The time-resolved emission spectra (TRES) of mCP:PO acceptor:30% DMAC-DPS:0.5% 4CzTPNBu films were measured to examine the exact energy transfer process (Fig. 3b). In the time range of 100–500 ns, along with the decrease of the bands assigned to DMAC-DPS (~ 470 nm), the bands that peaked at ~ 500 nm gradually became dominant, which could be attributed to phosphorescence from the PO acceptors. After the coexistence of the phosphorescent and yellow bands during this time range, the yellow bands remained while the phosphorescence bands vanished. Furthermore, despite the low 4CzTPNBu concentration (0.5%), the DF lifetimes (τ_{DF}) of blue bands of DMAC-DPS singly doped films ($x = 0$) decreased from 1 to 0.5 μ s while the τ_{DF} values of yellow bands decreased to 0.7 μ s (Fig. 3c;

Supplementary Table 2). With a large distance between the dopants, energy transfer depends largely on the intermediate T_1 energy levels of the PO acceptors for exciton migration from blue to yellow dopants.

Apart from the ultrafast intensity rise (6 ns) in yellow bands (insets in Fig. 3c), we recorded appreciable and nearly synchronous rises in both phosphorescent and yellow bands within 100–500 ns. DMAC-DPS with high-lying excited states supports additional energy transfer to the T_1 state of the PO acceptor and then 4CzTPNBu. These synchronous rises further suggest coordination of the exciplex and DMAC-DPS in facilitating energy transfer to 4CzTPNBu. Therefore, upon excitation, a fast, singlet energy transfer occurs, and the triplet energy can be immediately transferred from the exciplexes to DMAC-DPS and then to the T_1 energy levels of the PO acceptors within 100–500 ns (Fig. 3d). Almost instantly, the PO acceptors provide the triplet-exciton migration and energy transfer to 4CzTPNBu. As a result, energy harvesting is improved by energy relaying that occurs between blue and yellow dyes, namely mCP:PO acceptor \rightarrow DMAC-DPS \rightarrow PO acceptor \rightarrow 4CzTPNBu.

WOLED performance. Based on the high ϕ_{PL} values of dual-doped exciplex films and the excellent electrical performance of the PO acceptors and their exciplexes (Supplementary Fig. 3; Supplementary Tables 1 and 2), we further constructed two trilayer TADF-based WOLEDs (W1 and W2) with doubly doped, single-emissive layers (Fig. 4a; Supplementary Fig. 6). Through concentration tuning of 4CzTPNBu, we achieved color modulation from pure white to warm white with a color rendering index beyond 80 and with high chromatic stability (Fig. 4b; Supplementary Figs. 7 and 8; Supplementary Table 3). Commission Internationale de l’Eclairage (CIE) coordinates and correlated color temperatures were (0.31, 0.35)/6582 K for the pure white device and (0.44, 0.47)/3474 K for the warm white device. Their chromatic purity compared well with a standard daylight source (Illuminant D65) and an incandescent light (Illuminant A).

For the mCP:pDPBITPO-based device W1, we achieved maximum efficiencies of 98.4 lm W^{-1} and 30.6%. mCP:DpPBITPO-derived W2 generated a power efficiency of 108.2 lm W^{-1} , an external quantum efficiency of 32.7% and a device lifetime of 233 h at half-initial luminance (Fig. 4c; Supplementary Figs. 9–11). Device degradation is mainly due to photo- and electro-decomposition of DMAC-DPS (Supplementary Figs. 12 and 13). So, using another more stable blue TADF emitter 4,5-bis(carbazol-9-yl)-1,2-dicyanobenzene (2CzPN) instead of DMAC-DPS (Supplementary Fig. 14), device lifetime can be doubled (Supplementary Fig. 11). Based on a 30% out-coupling ratio of an indium tin oxide glass, we derived 100% internal quantum efficiencies (η_{IQE}) for both W1 and W2. Large-size WOLEDs are hard to fabricate due to stringent requirements on defect control and device homogeneity. We next fabricated TADF WOLED prototypes with lateral dimensions of 8 cm \times 8 cm and efficiencies of 82.7 lm W^{-1} and 25.0% (Fig. 4d, Supplementary Fig. 15). Our approach is applicable to conventional acceptors. For example, devices W3 and W4, based on two commercial TPBI and BPhen acceptors, achieved maximum efficiencies of 71.3 lm W^{-1} and 22.6% (Fig. 4c, Supplementary Table 3). In addition, our strategy enabled phosphorescent and hyperfluorescent WOLEDs with respective external quantum efficiencies of 32.4% and 13.7% (Supplementary Fig. 16).

It is interesting that the maximum η_{EQE} values of W1 and W2 are larger than the sum of the corresponding singly doped blue and yellow devices (Supplementary Figs. 17 and 18). We further doped 30% DMAC-DPS in the emissive layer of the yellow device

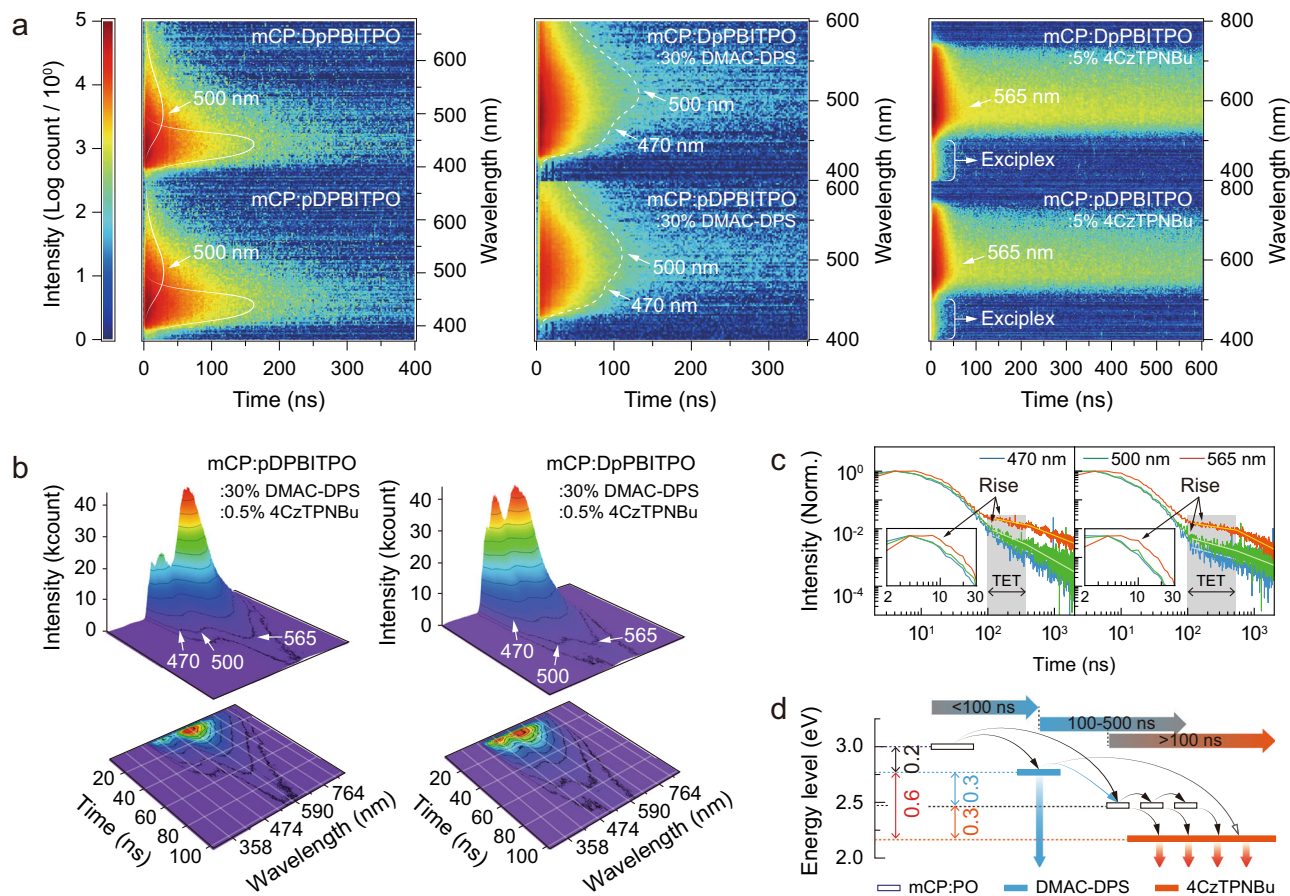


Fig. 3 Transient emission properties of the exciplexes and their TADF dye-doped films. **a** Time-dependent emission contours of mCP:pDPBITPO and mCP:DpPBITPO films, 30% DMAC-DPS-doped exciplex films and 4CzTPNBu-doped (5%) exciplex films, measured in the range of 350–600 nm. **b** Time-dependent emission intensity profiles of mCP:pDPBITPO and mCP:DpPBITPO films doped with 30 wt% DMAC-DPS and 0.5 wt% 4CzTPNBu within 120 ns after excitation. **c** Time-decay curves of mCP:pDPBITPO (left) and mCP:DpPBITPO (right) films doped with 30 wt.% DMAC-DPS and 0.5 wt% 4CzTPNBu. TET refers to a triplet energy transfer from DMAC-DPS to phosphine oxide (PO) acceptors. **d** Proposed time-dependent energy transfer processes in dually-doped exciplex films, showing a ladder-like energy relaying enabled by the low-lying T_1 energy level of the PO acceptor.

(Supplementary Fig. 19). Incorporation of DMAC-DPS dramatically improved the efficiencies by ~40%. Furthermore, we fabricated an mCP:DpPBITPO-based WOLED with dual emissive layers, in which DMAC-DPS and 4CzTPNBu were spatially separated to interrupt triplet energy transfer from DMAC-DPS to DpPBITPO to 4CzTPNBu. This reduced maximum efficiencies to 9.3%, due to triplet leakage to the T_1 levels of DpPBITPO in the blue-emissive layer and nonradiative energy loss in the yellow-emissive layer (Supplementary Fig. 20). Taken together, the exciplexes foster energy relaying between the blue and yellow dopants for high-efficiency white electroluminescence.

Discussion

Our work suggests a general approach to realizing single-emissive-layer TADF WOLEDs with fluorescent lamp efficiency. This strategy, based on exciplex hosts with energy levels simultaneously matching those of blue and yellow dopants, enables a ladder-like, high-efficiency energy relaying. Implementation of these exciplex hosts leads to 100% exciton harvesting. Furthermore, the realization of purely TADF-based WOLEDs in a simple trilayer device provides a sustainable, cost-effective approach to mitigating fabrication complexity. Ultimately, our molecular design may offer fundamental insight into energy transfer in multicomponent white-emitting systems and add value to the construction of next-generation lighting sources.

Methods

Preparation of PO acceptors. We designed and synthesized two phosphine oxide acceptors (pDPBITPO and DpPBITPO). These acceptors were fully characterized by ¹H NMR, ¹³C NMR, ³¹P NMR, MS, elemental analysis, and single-crystal (if available) X-ray diffraction analysis (Supplementary Figs 21–26).

General procedure of the cyclization reaction. In an argon atmosphere, aromatic aldehyde (1 mmol) and arylamine (1 mmol) were dissolved in DMF (5 mL). The resulting solution was heated to 80 °C. A saturated aqueous Na₂S₂O₅ solution (1 mL) was then added to the mixture and stirred for 20 h at 80 °C. After cooling to room temperature, the mixture was poured into water. The precipitate was filtered as a crude product and further recrystallized with methanol to afford phenylbenzimidazole derivatives.

2-(4-Bromophenyl)-1-(3,5-dibromophenyl)-1H-benzo[d]imidazole (pDPBITBr). prepared from 4-bromobenzaldehyde and *N*-(3,5-dibromophenyl)benzene-1,2-diamine to afford white powder in 73% yield. ¹H NMR (TMS, CDCl₃, 400 MHz): 7.880 (d, *J* = 8.0 Hz, 1H), 7.809 (m, 1H), 7.532 (d, *J* = 8.4 Hz, 2H), 7.454 (d, *J* = 8.8 Hz, 4H), 7.388 (t, *J* = 7.2 Hz, 1H), 7.36 (t, *J* = 7.2 Hz, 1H), 7.259 ppm (d, *J* = 8.0 Hz, 1H); ¹³C NMR (TMS, CDCl₃, 100 MHz): 149.900, 141.878, 137.911, 135.705, 133.655, 130.916, 129.751, 128.253, 127.122, 123.642, 123.131, 122.843, 122.730, 119.244, 109.057 ppm; HRMS (MALDI-TOF) *m/z*: [M + H⁺] 506.875; elemental analysis (%) for C₁₉H₁₁Br₃N₂: C 45.01, H 2.19, N 5.53; found: C 45.03, H 2.18, N 5.55.

1-(4-Bromophenyl)-2-(3,5-dibromophenyl)-1H-benzo[d]imidazole (DpPBITBr). prepared from 3,5-dibromobenzaldehyde and *N*-(4-bromophenyl)benzene-1,2-diamine to afford white powder in 71% yield. ¹H NMR (TMS, CDCl₃, 400 MHz): 7.889 (d, *J* = 7.6 Hz, 1H), 7.712 (d, *J* = 8.4 Hz, 2H), 7.676 (t, *J* = 1.6 Hz, 1H), 7.644 (d, *J* = 1.6 Hz, 2H), 7.395 (td, *J* = 7.6 Hz, 1.2 Hz, 1H), 7.337 (td, *J* = 7.6 Hz, 1.2 Hz, 1H), 7.244–7.175 ppm (m, 3H); ¹³C NMR (TMS, CDCl₃, 100 MHz): 147.946,

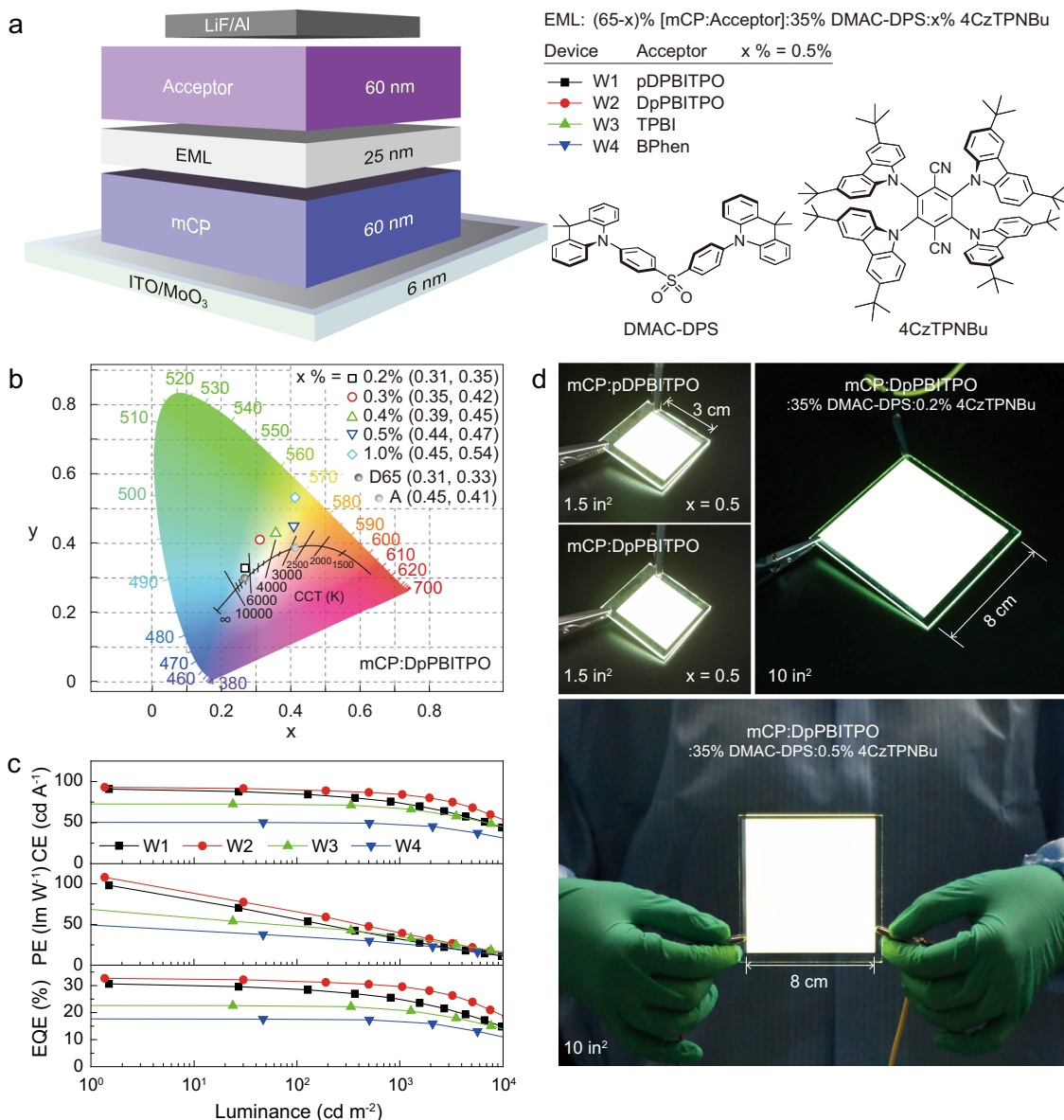


Fig. 4 Electroluminescence characterizations of single-emissive-layer TADF WOLEDs comprising ladder-like energy-relaying exciplexes. **a** An illustration showing device configuration, the emissive layer components of mCP:pDPBITPO- and mCP:DpPBITPO-hosted white TADF devices, and molecular structures of the doped dye emitters. **b** Commission International de l'Éclairage (CIE) coordinates of mCP:DpPBITPO-hosted TADF WOLEDs, fabricated with mCP:DpPBITPO:35% DMAC-DPS:x%4CzTPNBu. Their chromaticity is comparable to that of a standard daylight source (Illuminant D65) or an incandescent light (Illuminant A). **c** Efficiency vs. luminance measurements of the devices based on 35% DMAC-DPS and 0.5% 4CzTPNBu codoped mCP:pDPBITPO (W1), mCP:DpPBITPO (W2), mCP:TPBI (W3) and mCP:BPhen (W4). **d** Photographs of mCP:pDPBITPO- and mCP:DpPBITPO-hosted WOLED prototypes with lateral dimensions of 3 cm × 3 cm (1.5 inch²) and 8 cm × 8 cm (10 inch²).

141.754, 135.966, 134.279, 134.031, 132.437, 131.971, 129.887, 127.821, 123.335, 122.678, 122.055, 121.942, 119.321, 109.379 ppm; HRMS (MALDI-TOF) *m/z*: [M + H⁺] 506.875; elemental analysis (%) for C₁₉H₁₁Br₃N₂: C 45.01, H 2.19, N 5.53; found: C 45.02, H 2.19, N 5.56.

General procedure of phosphorylation. In an argon atmosphere, bromide (1 mmol), NaOAc (3.3 mmol), Pd(OAc)₂ (0.15 mmol) and diphenylphosphine (3.3 mmol) were dissolved in DMF (10 mL). The mixture was heated to 130 °C and kept at this temperature for 36 h under stirring. After cooling to room temperature, the reaction was quenched with water (20 mL). The solution was then extracted with CH₂Cl₂ (3 × 20 mL). The organic layers were combined and dried with anhydrous sodium sulfate. The solvent was removed *in vacuo* to afford phosphine precursors. Then, the phosphines were dissolved in CH₂Cl₂ (10 mL) and H₂O₂ (30%, 3 mL) was added to the CH₂Cl₂ solution dropwise at 0 °C. The mixture was stirred for 2 h, followed by extraction with CH₂Cl₂ (3 × 10 mL). The organic layers were combined and dried with anhydrous sodium sulfate. The solvent was removed

in vacuo, and the residue was purified by flash column chromatography to afford phosphine oxide derivatives.

(5-(2-(4-(Diphenylphosphoryl)phenyl)-1H-benzo[d]imidazol-1-yl)-1,3-phenylene)bis(diphenylphosphine oxide) (pDPBITPO), prepared from pDPBITBr to afford white powder in 67% yield. ¹H NMR (TMS, CDCl₃, 400 MHz): 7.878-7.757 (m, 4H), 7.723 (dd, *J*₁ = 8.0 Hz, *J*₂ = 11.6 Hz, 2H), 7.653 (dd, *J*₁ = 8.0 Hz, *J*₂ = 11.6 Hz, 4H), 7.584-7.518 (m, 5H), 7.518-7.418 (m, 15H), 7.418-7.343 (m, 8H), 7.343-7.291 (m, 1H), 7.258 (t, *J* = 7.6 Hz, 1H), 7.065 ppm (d, *J* = 8.0 Hz, 1H); ¹³C NMR (TMS, CDCl₃, 100 MHz): 149.765, 141.950, 136.643, 136.531, 136.472, 136.338, 135.668, 135.555, 135.386, 134.038, 133.941, 133.847, 133.802, 132.789, 132.618, 132.535, 131.878, 131.850, 131.581, 131.274, 131.226, 131.199, 131.178, 131.053, 130.953, 130.763, 130.711, 130.660, 130.548, 130.200, 129.148, 128.474, 128.355, 127.924, 127.859, 127.796, 127.754, 127.632, 123.410, 122.848, 119.402, 109.656 ppm; ³¹P NMR (TMS, CDCl₃, 160 MHz): 28.195, 27.637 ppm; HRMS (MALDI-TOF) *m/z*: [M + H⁺] 871.323; elemental analysis (%) for C₅₅H₄₁N₂O₃P₃: C 75.86, H 4.75, N 3.22; found: C 75.88, H 4.76, N 3.25.

(5-(1-(4-(Diphenylphosphoryl)phenyl)-1H-benzo[d]imidazol-2-yl)-1,3-phenylene)bis(diphenylphosphine oxide) (DpPBITPO). prepared from DpPBITBr to afford white powder in 69% yield. ^1H NMR (TMS, CDCl_3 , 400 MHz): 8.109 (d, $J = 12.4$ Hz, 2H), 7.901 (t, $J = 11.2$ Hz, 1H), 7.841–7.744 (m, 3H), 7.730 (dd, $J_1 = 7.6$ Hz, $J_2 = 12.0$ Hz, 4H), 7.577 (m, 2H), 7.539–7.430 (m, 16H), 7.421–7.302 (m, 9H), 7.302–7.241 (m, 3H), 7.191 ppm (d, $J = 8.0$ Hz, 1H); ^{13}C NMR (TMS, CDCl_3 , 100 MHz): 148.973, 141.925, 138.369, 138.339, 135.757, 135.039, 134.937, 134.908, 134.829, 134.798, 134.261, 134.156, 133.272, 133.187, 133.161, 133.122, 133.057, 132.952, 132.264, 131.309, 131.234, 131.146, 131.046, 130.917, 130.866, 130.814, 130.702, 130.188, 129.656, 127.884, 127.794, 127.762, 127.734, 127.668, 126.195, 126.072, 123.349, 122.737, 119.345, 109.388 ppm; ^{31}P NMR (TMS, CDCl_3 , 160 MHz): 28.437, 27.966 ppm; HRMS (MALDI-TOF) m/z : $[\text{M} + \text{H}^+]$ 871.351; elemental analysis (%) for $\text{C}_{55}\text{H}_{41}\text{N}_2\text{O}_3\text{P}_2$: C 75.86, H 4.75, N 3.22; found: C 75.88, H 4.76, N 3.25.

DFT calculations. DFT computations were performed with different parameters for structural optimization and vibrational analysis. The ground state configuration of DpPBITPO was established according to single-crystal data. Ground, singlet, and triplet states in vacuum were optimized by restricted and unrestricted formalisms of Beck's three-parameter hybrid exchange functional³² and Lee, and Yang and Parr correlation functional³³ B3LYP/6-31 G(d,p), respectively. Fully optimized stationary points were further characterized by harmonic vibrational frequency analysis to ensure a real, local minimum without imaginary vibrational frequency. Total energies were also corrected using zero-point energy for both the ground and triplet states. Contours were visualized using Gaussview 5.0. All computations were performed using a Gaussian 09 software package.

Device fabrication and testing. Before loading into a deposition chamber, the ITO substrate was cleaned with detergent and deionized water, dried in an oven at 120 °C for 4 h, and treated with oxygen plasma for 3 min. Devices were fabricated by evaporating organic layers at a rate of 0.1–0.2 nm s^{-1} onto the ITO substrate sequentially at a pressure below 4×10^{-4} Pa. Onto the electron-transporting layer, a layer of LiF with 1-nm thickness was deposited at a rate of 0.1 nm s^{-1} to improve electron injection. Finally, a 100-nm layer of Al was deposited at a rate of 0.6 nm s^{-1} as the cathode. The emission area of the devices was 0.09 cm^2 , as determined by the overlapped area of the anode and the cathode. After fabrication, devices were immediately transferred to a glove box for encapsulation with glass coverslips using epoxy glue. EL spectra and CIE coordinates were measured using a PR655 spectrum colorimeter. Current–density–voltage and brightness–voltage curves of the devices were measured using a Keithley 4200 source meter and a calibrated silicon photodiode. All measurements were carried out at room temperature under ambient conditions. For each structure, four devices were fabricated in parallel to confirm performance repeatability. The data reported herein were those closest to the average results.

Photophysical measurement. Steady-state emission spectra were measured using an Edinburgh FPLS 920 fluorescence spectrophotometer. TADF dye-doped films (100 nm) were prepared by vacuum evaporation for optical analysis. Photoluminescence quantum yields (PLQY , ϕ_{PL}) of these films were measured through a Labsphere 1-M-2 ($\phi = 6^\circ$) integrating sphere coated with Benflect having efficient light reflection from 200 to 1600 nm, which was integrated with FPLS 920. The absolute ϕ_{PL} determination of the sample was performed with two spectral (emission) scans, with the emission monochromator scanning over the Rayleigh scattered light from the sample and a blank substrate. The first spectrum recorded the scattered light and the sample emission, and the second spectrum recorded the scattered light of the Benflect coating. Integration and subtraction of the scattered light in the two spectra are equal to the number of photons absorbed by the samples (N_a), while integration of the sample emission is equal to the number of photons emitted (N_e). Then, absolute ϕ_{PL} can be estimated according to the equation of $\phi_{\text{PL}} = N_e/N_a$. Spectral correction (emission arm) was applied to raw data after background subtraction, and from these spectrally corrected curves, the quantum yield was calculated using an F900 software wizard.

Time-resolved photoluminescence measurements with nanosecond time resolution were acquired with a gated, intensified CCD camera system (Andor iStar DH740 CCI-010) connected to a grating spectrometer (Andor SR303i) at room temperature. Excitation (wavelength: 350 nm) was performed with femtosecond laser pulses, generated by introducing 1 kHz pulses (pulse length: 80 fs) from a central Ti:sapphire amplifier system (Spectra-Physics Solstice) to a TOPAS optical parametric amplifier (Light Conversion). Time-resolved photoluminescence of the sample was obtained by stepping the intensified CCD gate delay relative to the pump pulse. The gate width was 2 ns.

Data availability

Data that support the findings of this study are available from the corresponding authors upon request. The X-ray crystallographic coordinates for the DpPBITPO structure reported in this study have been deposited at the Cambridge Crystallographic Data Centre (CCDC), under deposition numbers 2077630. These data can be obtained free of charge from The Cambridge Crystallographic Data Centre via www.ccdc.cam.ac.uk/data_request/cif.

Received: 5 March 2021; Accepted: 14 May 2021;

Published online: 15 June 2021

References

- Kido, J., Kimura, M. & Nagai, K. Multilayer white light-emitting organic electroluminescent device. *Science* **267**, 1332–1334 (1995).
- Sun, Y. R. et al. Management of singlet and triplet excitons for efficient white organic light-emitting devices. *Nature* **440**, 908–912 (2006).
- Reineke, S. et al. White organic light-emitting diodes with fluorescent tube efficiency. *Nature* **459**, 234–238 (2009).
- Uoyama, H., Goushi, K., Shizu, K., Nomura, H. & Adachi, C. Highly efficient organic light-emitting diodes from delayed fluorescence. *Nature* **492**, 234–238 (2012).
- Tao, Y. et al. Thermally activated delayed fluorescence materials towards the breakthrough of organoelectronics. *Adv. Mater.* **26**, 7931–7958 (2014).
- Ahn, D. H. et al. Highly efficient blue thermally activated delayed fluorescence emitters based on symmetrical and rigid oxygen-bridged boron acceptors. *Nat. Photon* **13**, 540–546 (2019).
- D'Andrade, B. W. & Forrest, S. R. White organic light-emitting devices for solid-state lighting. *Adv. Mater.* **16**, 1585–1595 (2004).
- Kamtekar, K. T., Monkman, A. P. & Bryce, M. Recent advances in white organic light-emitting materials and devices (WOLEDs). *Adv. Mater.* **22**, 572–584 (2010).
- Yu, L. et al. Red, green, and blue light-emitting polyfluorenes containing a dibenzothiophene-S,S-dioxide unit and efficient high-color-rendering-index white-light-emitting diodes made therefrom. *Adv. Funct. Mater.* **23**, 4366–4376 (2013).
- Wang, Q. & Ma, D. Management of charges and excitons for high-performance white organic light-emitting diodes. *Chem. Soc. Rev.* **39**, 2387–2398 (2010).
- Zhao, F. et al. Spatial exciton allocation strategy with reduced energy loss for high-efficiency fluorescent/phosphorescent hybrid white organic light-emitting diodes. *Mater. Horiz.* **4**, 641–648 (2017).
- Cui, L. S. et al. Controlling synergistic oxidation processes for efficient and stable blue thermally activated delayed fluorescence devices. *Adv. Mater.* **28**, 7620–7625 (2016).
- Jankus, V. et al. Highly efficient TADF OLEDs: how the emitter-host interaction controls both the excited state species and electrical properties of the devices to achieve near 100% triplet harvesting and high efficiency. *Adv. Funct. Mater.* **24**, 6178–6186 (2014).
- Han, C., Zhang, Z., Ding, D. & Xu, H. Dipole-dipole interaction management for efficient blue thermally activated delayed fluorescence diodes. *Chemistry* **4**, 2154–2167 (2018).
- Fan, C. et al. Dibenzothiophene-based phosphine oxide host and electron-transporting materials for efficient blue thermally activated delayed fluorescence diodes through compatibility optimization. *Chem. Mater.* **27**, 5131–5140 (2015).
- Liu, Y., Li, C., Ren, Z., Yan, S. & Bryce, M. R. All-organic thermally activated delayed fluorescence materials for organic light-emitting diodes. *Nat. Rev. Mater.* **3**, 18020 (2018).
- Wu, Z. et al. Strategic-tuning of radiative excitons for efficient and stable fluorescent white organic light-emitting diodes. *Nat. Commun.* **10**, 2380 (2019).
- Li, Y. et al. Design strategy of blue and yellow thermally activated delayed fluorescence emitters and their all-fluorescence white OLEDs with external quantum efficiency beyond 20%. *Adv. Funct. Mater.* **26**, 6904–6912 (2016).
- Zhang, B. et al. High-efficiency single emissive layer white organic light-emitting diodes based on solution-processed dendritic host and new orange-emitting iridium complex. *Adv. Mater.* **24**, 1873–1877 (2012).
- Zhang, Q. et al. Efficient blue organic light-emitting diodes employing thermally activated delayed fluorescence. *Nat. Photon.* **8**, 326–332 (2014).
- Förster, T. Zwischenmolekulare energiewanderung und fluoreszenz. *Ann. Phys. (Berl.)* **437**, 55–75 (1948).
- Dexter, D. L. A theory of sensitized luminescence in solids. *J. Chem. Phys.* **21**, 836–850 (1953).
- Xu, H. & Huang, W. Spectroscopic study of intramolecular energy transfer in a phosphine oxide Eu^{3+} complex: a stepwise process induced by intermediate energy levels. *J. Photochem. Photobiol. A* **217**, 213–218 (2011).
- Sun, J. et al. Charge-transfer exciton manipulation based on hydrogen bond for efficient white thermally activated delayed fluorescence. *Adv. Funct. Mater.* **30**, 1908568 (2020).
- Ding, D. et al. Highly efficient and color-stable thermally activated delayed fluorescence white light-emitting diodes featured with single-doped single emissive layers. *Adv. Mater.* **32**, 1906950 (2020).
- Feng, J. & Zhang, H. Hybrid materials based on lanthanide organic complexes: a review. *Chem. Soc. Rev.* **42**, 387–410 (2013).

27. Wang, Z. et al. The application of charge transfer host based exciplex and thermally activated delayed fluorescence materials in organic light-emitting diodes. *Org. Electron.* **66**, 227–241 (2019).
28. Duan, C., Han, C., Du, R., Wei, Y. & Xu, H. High-efficiency blue dual-emissive exciplex boosts full-radiative white electroluminescence. *Adv. Opt. Mater.* **6**, 1800437 (2018).
29. Liu, X.-K. et al. Prediction and design of efficient exciplex emitters for high-efficiency, thermally activated delayed-fluorescence organic light-emitting diodes. *Adv. Mater.* **27**, 2378–2383 (2015).
30. Gibson, J., Monkman, A. P. & Penfold, T. J. The importance of vibronic coupling for efficient reverse intersystem crossing in thermally activated delayed fluorescence molecules. *ChemPhysChem* **17**, 2956–2961 (2016).
31. Chaudhuri, D. et al. Metal-free OLED triplet emitters by side-stepping Kasha's rule. *Angew. Chem. Int. Ed.* **52**, 13449–13452 (2013).
32. Becke, A. D. Density-functional thermochemistry. III. The role of exact exchange. *J. Chem. Phys.* **98**, 5648–5652 (1993).
33. Lee, C., Yang, W. & Parr, R. G. Development of the Colle-Salvetti correlation-energy formula into a functional of the electron density. *Phys. Rev. B* **37**, 785–789 (1988).

Acknowledgements

This project was financially supported by the Changjiang Scholar Program of the Chinese Ministry of Education (Q2016208), the National Natural Science Foundation of China (92061205, U1801258, 51873056 and 22005088), the National Basic Research Program of China (973 Program, 2015CB932200), and National Research Foundation, Prime Minister's Office, Singapore under its Investigatorship Award Program (NRF-NRFI05-2019-0003).

Author contributions

C.H. and R.D. contributed equally to this work. W.H., X.L., and H.X. conceived the projects. C.H., R.D., S.H., P.M., J.B., M.S., C.D., and Y.W. performed the experiments. C.H., R.D., S.H., H.X., X.L., and W.H. analyzed the data and wrote the paper. All authors commented on the manuscript.

Competing interests

The authors declare no competing interests.

Additional information

Supplementary information The online version contains supplementary material available at <https://doi.org/10.1038/s41467-021-23941-z>.

Correspondence and requests for materials should be addressed to H.X., X.L. or W.H.

Peer review information *Nature Communications* thanks Sebastian Reineke and the other, anonymous, reviewer(s) for their contribution to the peer review of this work.

Reprints and permission information is available at <http://www.nature.com/reprints>

Publisher's note Springer Nature remains neutral with regard to jurisdictional claims in published maps and institutional affiliations.



Open Access This article is licensed under a Creative Commons Attribution 4.0 International License, which permits use, sharing, adaptation, distribution and reproduction in any medium or format, as long as you give appropriate credit to the original author(s) and the source, provide a link to the Creative Commons license, and indicate if changes were made. The images or other third party material in this article are included in the article's Creative Commons license, unless indicated otherwise in a credit line to the material. If material is not included in the article's Creative Commons license and your intended use is not permitted by statutory regulation or exceeds the permitted use, you will need to obtain permission directly from the copyright holder. To view a copy of this license, visit <http://creativecommons.org/licenses/by/4.0/>.

© The Author(s) 2021